RESEARCH ARTICLE

LASER & PHOTONICS REVIEWS

www.lpr-journal.org

High-Efficiency Label-Free 3D Microscopy Using Kramers-Kronig Relations-Assisted Fourier Ptychographic Diffraction Tomography

Zhidong Bai, Shun Zhou, Linpeng Lu, Habib Ullah, Ran Ye, Qian Chen, and Chao Zuo**

A high-efficiency 3D refractive index (RI) tomography method is presented, termed Kramers–Kronig relations-assisted Fourier ptychographic diffraction tomography (KK-FPDT). This approach integrates the spatial-domain Kramers–Kronig (KK) relations with Fourier ptychographic diffraction tomography (FPDT), enabling high-quality RI reconstruction from intensity images captured under both matched and non-matched illuminations. By leveraging KK relations, the initial 3D scattering potential spectrum is generated deterministically, which significantly accelerates convergence in the subsequent iterative FPDT reconstruction process. KK-FPDT overcomes the limitations of conventional KK-ODT methods, which are constrained by matched illumination conditions, thereby improving spectral coverage and reconstruction quality significantly. Experiments on microspheres, resolution targets, and biological samples (including 3T3 cells and *Pandorina morum*) validated KK-FPDT's capability for high-resolution 3D RI imaging with 340 nm lateral resolution. KK-FPDT offers a robust and versatile solution for label-free quantitative analysis of cellular and tissue morphology, paving the way for broader biomedical applications.

1. Introduction

Optical diffraction tomography (ODT) has emerged as a promising label-free 3D microscopic technique, offering detailed 3D visualization of subcellular structures and enabling deeper insights into cellular functions and biological processes.[1–8] By eliminating the need for interferometric configuration, non-interferometric ODT reconstructs the 3D refractive index (RI) distribution of biological specimens from intensity-only measurements. This approach has garnered increasing attention due to its simplified optical system, speckle-free image quality, and high compatibility with conventional optical microscopes. In recent years, significant efforts have been devoted to the development of various non-interferometric ODT techniques, which are primarily categorized into intensity diffraction tomography based on angular illumination scanning[9–14] and transport-of-intensity diffraction tomography based on z-axis scanning.[15–20] These approaches are typically implemented under the weak-object approximation (e.g., first-order Born or Rytov approximations) to establish linear relationships between the measured intensity images and the object's scattering potential.[21,22] Recent advancements have introduced multi-layer beam propagation method and deep learning-based strategies to address the challenges posed by multiple scattering, facilitating more precise RI reconstruction in complex biological specimens with strong scattering.[23–29]

Fourier ptychographic diffraction tomography (FPDT), a typical non-interferometric ODT technique, enables wide-field, high-resolution, and depth-resolved complex RI tomography by synthesizing numerous low-resolution intensity images acquired under variable-angle illumination in Fourier space.[13,30] However, due to the loss of phase information inherent in intensity-only measurements, FPDT requires iterative phase retrieval to reconstruct the 3D RI distribution of the sample. This iterative process is computationally intensive and time-consuming, thereby limiting the practical applicability and widespread adoption of FPDT.[31] A recent study by Park et al. proposed an intensity-based holographic ODT technique via spatial-domain Kramers-Kronig (KK) relations (KK-ODT).[32] KK-ODT enables direct recovery of the complex amplitude of the scattered

Z. Bai, S. Zhou, L. Lu, H. Ullah, R. Ye, C. Zuo
Smart Computational Imaging Laboratory (SCILab)
School of Electronic and Optical Engineering
Nanjing University of Science and Technology
Nanjing, Jiangsu Province 210094, China
E-mail: zuochao@njust.edu.cn

Z. Bai, S. Zhou, L. Lu, H. Ullah, C. Zuo
Smart Computational Imaging Research Institute (SCIRI) of Nanjing University of Science and Technology
Nanjing, Jiangsu Province 210019, China

Z. Bai, S. Zhou, L. Lu, H. Ullah, Q. Chen, C. Zuo
Jiangsu Key Laboratory of Visual Sensing & Intelligent Perception
Nanjing, Jiangsu Province 210094, China
E-mail: chenqian@njust.edu.cn

Q. Chen, C. Zuo
State key Laboratory of Extreme Environment Optoelectronic Dynamic Measurement Technology and Instrument
Taiyuan, Shanxi Province 030051, China

R. Ye
School of Computer and Electronic Information
Nanjing Normal University
Nanjing 210023, China

The ORCID identification number(s) for the author(s) of this article can be found under https://doi.org/10.1002/lpor.202500705

DOI: 10.1002/lpor.202500705

field from oblique illumination intensity images by leveraging the KK relations without the need for iterative computations. However, the application of KK relations requires strict adherence to the analyticity condition,[32,33] which demands precise matching between the numerical apertures (NAs) of the illumination and the objective lens.[32,34] This requirement limits the illumination scheme to NA-matched annular patterns, resulting in a reduced filling ratio of the scattering potential spectrum and ultimately compromising the quality of RI reconstruction.

We recently established a unified theoretical framework linking the optical transfer function (OTF) with the space-domain KK relations.[35,36] Within this framework, the analyticity condition required by the KK relations is interpreted through OTF theory, offering a potential pathway to relax the stringent matched illumination condition. Under oblique illumination, the phase optical transfer function (POTF) associated with the recorded intensity image comprises two laterally shifted, anti-symmetric pupils. When the illumination NA precisely matches that of the objective lens, these two pupils become tangent, enabling full transfer of low-frequency phase information to the intensity image. This condition is equivalent to satisfying the analyticity requirement of the KK relations. As the illumination angle decreases, the two anti-symmetric pupils increasingly overlap in the low-frequency region, leading to partial or complete cancellation and consequent loss of low-frequency phase information.[35,37] From the perspective of KK relations, such non-matched illumination violates the analyticity condition, rendering the KK approach inapplicable. However, analysis via POTF reveals that the non-overlapping high-frequency regions remain effective in conveying phase information. These retained components can potentially be exploited to supplement the scattering potential spectrum, thereby enabling full-angle illumination to improve the quality of RI tomographic reconstruction.

Here, we propose a novel non-interferometric 3D RI tomography method, termed Kramers–Kronig relations-assisted Fourier ptychographic diffraction tomography (KK-FPDT). KK-FPDT combines the high-efficiency scattered field estimation enabled by the KK relations with the intensity consistency constraint of FPDT, allowing high-quality RI reconstruction from intensity images acquired under both matched and non-matched illumination conditions. By leveraging the KK relations, an initial 3D scattering potential spectrum is deterministically generated, which significantly accelerates the convergence in the subsequent iterative FPDT reconstruction process. KK-FPDT overcomes the limitations of conventional KK-ODT methods that require strictly matched illumination, thereby substantially improving spectral coverage and reconstruction quality. Experimental results on standard microspheres, resolution target and biological specimens (including 3T3 cells and *Pandorina morum*) demonstrate the capability of KK-FPDT to achieve high-resolution 3D RI imaging with a lateral resolution of 340 nm. These results indicate that KK-FPDT is a robust and versatile solution for label-free, quantitative analysis of cellular and tissue morphology, paving the way for broader applications in biomedical imaging and diagnostics.

2. Methods

2.1. Principle of Diffraction Tomography

The implementation of FPDT is based on the well-known Fourier diffraction theorem.[38,39] As illustrated in **Figure 1a**, when an object $V(\mathbf{r})$ is illuminated by monochromatic plane wave $U_{in}(\mathbf{r})$, the generated first-order scattered field $U_{s1}(\mathbf{r})$ satisfies the linear relationship with the object function $V(\mathbf{r})$, which can be expressed in the Fourier domain as follows (see the detailed derivation in Supporting Information S1):

$$\hat{V}(\mathbf{k}-\mathbf{k}_{in}) = -4\pi j k_z \hat{U}_{s1}(\mathbf{k}_T) P(\mathbf{k}) \tag{1}$$

where $\mathbf{k} = (\mathbf{k}_T, k_z) = (k_x, k_y, k_z)$ is the 3D spatial frequency coordinates corresponding to $\mathbf{r} = (\mathbf{r}_T, r_z) = (r_x, r_y, r_z)$. $\mathbf{k}_{in}$ is the wave vector of the incident field. $\hat{V}(\mathbf{k})$ and $\hat{U}_{s1}(\mathbf{k}_T)$ correspond to the 3D and 2D Fourier transforms of $V(\mathbf{r})$ and $U_{s1}(\mathbf{r}_T)$, respectively. $U_{s1}(\mathbf{r}_T)$ can be obtained from the total field $U(\mathbf{r}_T)$ using either the first-order Born or Rytov approximation (See Supporting Information S1). $P(\mathbf{k}) = P(\mathbf{k}_T)\delta\left(k_z - \sqrt{k_m^2 - |\mathbf{k}_T|^2}\right)$ called 3D coherent transfer function is obtained by projecting the 2D $P(\mathbf{k}_T)$ to 3D space (See Supporting Information S1). For interferometric ODT, the complex amplitude distribution of $U(\mathbf{r}_T)$ is initially measured via interferometry. Subsequently, the first-order scattered field $U_{s1}(\mathbf{r}_T)$ is calculated according to Equation (S10) and is mapped onto the $\hat{V}(\mathbf{k})$ at the appropriate position in Fourier space. As a non-interferometric ODT method, FPDT reconstructs the 3D RI distribution from the intensity-only measurements. Therefore, it is essential to establish a relationship between the recorded intensity images and the sample's scattering potential. Given its superior applicability for imaging thick biological samples compared to the Born approximation, the Rytov approximation was adopted in this work.[21,40] Under this approximation, the measured intensity at the camera's detection plane can be expressed as follows:

$$I = \left| U_{in} \exp\left(\frac{U_{s1}}{U_{in}}\right)\right|^2 \tag{2}$$

Previous FPDT techniques require the acquisition of a large number of intensity images under varying illumination angles to ensure sufficient data redundancy. Subsequently, multiple time-consuming iterative updates are performed to ensure the convergence of the scattering potential during reconstruction, ultimately yielding the RI distribution.

2.2. Understand the KK Relations Under Full-Angle Illumination From the Perspective of the POTF

In KK-ODT, if the scattered field $\log[U(\mathbf{r}_T)]$ is analytic in the upper half-plane of $\mathbf{r}_T$, the phase of scattered field can be retrieved from the intensity using KK relations

$$\mathrm{Im}\{\log[U(\mathbf{r}_T)]\} = -\frac{1}{\pi} p \cdot v \cdot \int_{-\infty}^{\infty} \frac{\mathrm{Re}\left\{\log\left[U(\mathbf{r}'_T)\right]\right\}}{\mathbf{r}'_T - \mathbf{r}_T} d\mathbf{r}'_T \tag{3}$$

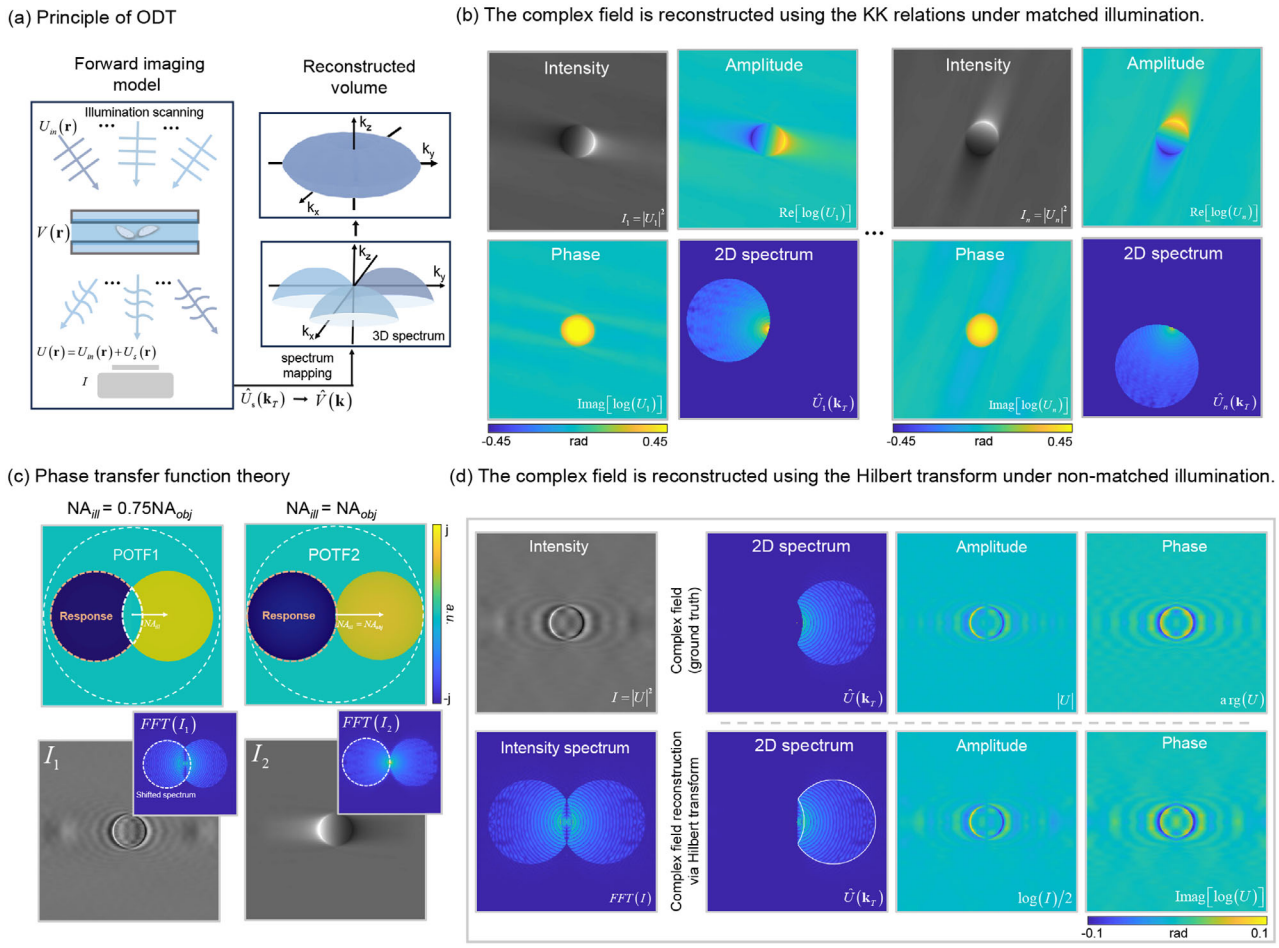

Figure 1. Principles of ODT based on KK relations. a) ODT principle: forward imaging model and reconstruction. b) Total field U is reconstructed using KK relations. The intensity image is converted into the phase image via KK relations under matched illumination. c) POTF theory. Intensity images measured at two different NA_{ill} and the corresponding phase transfer functions. d) Total field U is reconstructed using Hilbert transform under non-matched illumination.

where *p.v.* is the Cauchy principal value. The real and imaginary parts of $\log[U(\mathbf{r}_T)]$ are the intensity component $\log(I)/2$ and the phase component of $U(\mathbf{r}_T)$, respectively, where $I = \left|[U(\mathbf{r}_T)]\right|^2$. To ensure the analyticity of $\log[U(\mathbf{r}_T)]$ in the upper half-plane of $\mathbf{r}_T$, the illumination NA (NA_{ill}) must match the objective lens NA (NA_{obj}) (see the full derivation in Supporting Information S2). Figure 1b validates the phase retrieval capability of the KK relations under matched illumination. It is evident that KK relations can reconstruct the complete phase of the scattered field from the intensity image under any matched illumination. Implementing synthetic aperture[41] on the phase information retrieved at different illumination angles enables tomographic reconstruction. However, the matched illumination condition in KK-ODT restricts the illumination pattern to an annular configuration matching the NA_{obj}, resulting in limited spectrum information of the scattering potential in 3D k-space and compromising the quality of the RI reconstruction.

To maximize access to the scattering potential spectrum, full-angle illumination should be employed, which inherently includes a large number of illumination vectors that do not satisfy the matched illumination condition. When the NA_{ill} is smaller than that of the NA_{obj}–thus violating the matching condition–the scattered field, in principle, no longer fulfills the analytical requirements of the KK relations. Nevertheless, the KK relations can still be applied to retrieve high-frequency spectral components of the scattered field. The effectiveness of this approach can be explained and demonstrated from the perspective of the POTF. In a standard focused imaging system illuminated by a quasi-coherent source with wave vector $\mathbf{k}_{in}$, the POTF consists of two anti-symmetric apertures, each shifted according to the angle of the incident illumination:

$$POTF(\mathbf{k}_T) = j\left[P(\mathbf{k}_T + \mathbf{k}_{in}) - P(\mathbf{k}_T - \mathbf{k}_{in})\right] \tag{4}$$

Figure 1c shows the distribution of POTF, intensity, and intensity spectrum under two different illumination NA cases. When $NA_{ill} = 0.75NA_{obj}$, the two anti-symmetric pupils of the POTF cancel each other out at low spatial frequencies. This cancellation hinders the transmission of low-frequency phase information to the intensity image, resulting in an image that primarily displays high-frequency contrast. However, we observe that in regions where POTF does not exhibit cancellation, phase information can

still be effectively transmitted. This implies that the spectral content corresponding to the non-zero regions of the POTF in the intensity spectrum accurately retains the spectral characteristics of the scattered field. Although low-frequency components are absent, the high-frequency components can still be deterministically extracted using the KK relations, providing a reliable initialization for reconstructing the scattering potential spectrum. When $NA_{ill} = NA_{obj}$, both low- and high-frequency components of the phase components are fully transferred to the intensity image, which is equivalent to satisfying the analyticity required by the KK relations. In this sense, the analyticity in the conventional KK relations can be regarded as a special case of the POTF theory under matched illumination condition. By leveraging the POTF framework, the applicability of the KK relation can be extended to scenarios involving non-matched illumination (note that we refer to the responses to the effectively transmitted spectral information). To verify the accuracy of the high-frequency component of the phase reconstructed using KK relations under non-matched illumination, we used the Hilbert transform to reconstruct the complex amplitude of a microsphere, as depicted in Figure 1d. Specifically, we first used the Fourier diffraction theorem [Equation (S6)] to generate the total scattered field spectrum $\hat{U}(\mathbf{k}_T)$ under non-matched illumination. We then extracted only the high-frequency spectral region according to the corresponding POTF and treated its corresponding amplitude and phase as the ground truth, as illustrated in the first row of Figure 1d. Then, we applied the Hilbert transform to the intensity image of the scattered field to reconstruct the amplitude and phase, as illustrated in the second row of Figure 1d. The results indicate that the high-frequency phase information can still be accurately recovered and closely matches the ground truth. This demonstrates the feasibility of using the KK relations to reconstruct the high-frequency components of the scattered field even under non-matched illumination.

We further evaluated the phase retrieval performance of the KK relations across different NA_{ill}/NA_{obj} ratios (See Supporting Information S3). The results show that when NA_{ill} is less than NA_{obj}, the recovery of low-frequency phase component is impaired, and this degradation becomes more pronounced as the ratio decreases. Nevertheless, in all cases, the high-frequency components that are effectively transmitted can still be accurately recovered. These components contain critical structural information of samples, providing essential support for the initial estimation of the scattering potential spectrum. Based on this insight, we developed KK relations-assisted Fourier ptychographic diffraction tomography. By deterministically generating an initial 3D scattering potential spectrum using the KK relations, the convergence of the iterative FPDT reconstruction process is significantly accelerated. Moreover, KK-FPDT overcomes the limitations of traditional KK-ODT, which is constrained by matched illumination condition, thereby substantially improving spectral coverage and further enhancing the reconstruction quality.

2.3. KK-FPDT Reconstruction Algorithm

The reconstruction framework of the KK-FPDT algorithm, shown in **Figure 2** and summarized in Supporting Video S1, alternates between the spatial and Fourier domains according to the following steps:

Step 1. Reconstruct the amplitude and phase of the total field $U(\mathbf{r}_T)$ using the KK relations. In our experiments, we sequentially captured N intensity images under incident fields with different illumination wave vectors $\mathbf{k}_{in}$. Then we used KK relations to reconstruct the amplitude and phase of the total field $U(\mathbf{r}_T)$ at each illumination angle.

Step 2. Under the Rytov approximation, the first-order scattered field $U_{s1}(\mathbf{r}_T)$ is obtained from the total field $U(\mathbf{r}_T)$.

Step 3. Initialize a discrete estimate of the $\hat{V}(\mathbf{k})$. Based on the Fourier diffraction theorem, we generate an initial RI distribution by mapping the first-order scattered field $U_{s1}(\mathbf{r}_T)$ to the scattering potential spectrum $\hat{V}(\mathbf{k})$ at the correct location in Fourier space.

Step 4. Performs intensity constraints on the estimated $\hat{V}(\mathbf{k})$. For an incident field with wave vector $\mathbf{k}_{in}^i$, we determine the sub-spectrum information of the corresponding support domain in the $\hat{V}(\mathbf{k})$ according to the 3D generalized aperture $P(\mathbf{k})$. The sub-region of $\hat{V}(\mathbf{k})$ is projected along the k_z direction according to Equation (S7) to obtain the 2D Fourier sub-spectrum $\hat{U}_{s1}^i(\mathbf{k}_T)$. The inverse Fourier transform is performed on $\hat{U}_{s1}^i(\mathbf{k}_T)$ to obtain the first-order scattered field $U_{s1}^i(\mathbf{r}_T)$. We convert $U_{s1}^i(\mathbf{r}_T)$ to the measured field $U^i(\mathbf{r}_T)$ according to Equation (S10), and enforce the intensity constraint using the measured I^i to obtain the updated first-order scattered field $\bar{U}_{s1}^i(\mathbf{r}_T)$. The update formula is

$$\bar{U}_{s1}^i(\mathbf{r}_T) = \ln\left\{\sqrt{I_c^i(\mathbf{r}_T)}\frac{\exp\left(U_{s1}^i(\mathbf{r}_T)\right)}{\left|\exp\left(U_{s1}^i(\mathbf{r}_T)\right)\right|}\right\} \tag{5}$$

Fourier transforming $\bar{U}_{s1}^i(\mathbf{r}_T)$ to the frequency domain, we locally update the corresponding sub-region of the 3D spectrum $\hat{V}(\mathbf{k})$ according to Equation (2). Next, we move to the next illumination angle, which corresponds to a new spectrum region. Step 4 is repeated for all N images, which completes a sub-iteration of the KK-FPDT algorithm. The entire iterative scheme is repeated for M cycles until the iteration of KK-FPDT converges within all intensity images.

Step 5. The inverse 3D Fourier transform is performed on the converged $\hat{\bar{V}}(\mathbf{k})$ to reconstruct the 3D RI distribution.

Taken together, KK-FPDT allows for fast and stable convergence due to the addition of initial estimates of the RI distribution.

3. Results

3.1. Validation of KK-FPDT on Simulations

We applied the KK-FPDT technique to reconstruct a pure phase microsphere and compared it with the traditional KK-ODT to demonstrate the high-quality imaging performance of the proposed method through numerical simulation. To evaluate the reconstruction performance of these two methods, we employed Equation (S7) as the forward imaging model to calculate the intensity images of microspheres under different illumination angles. In addition, to confirm the convergence performance of KK-FPDT, we also applied the KK-FPDT to simulated multicellu-

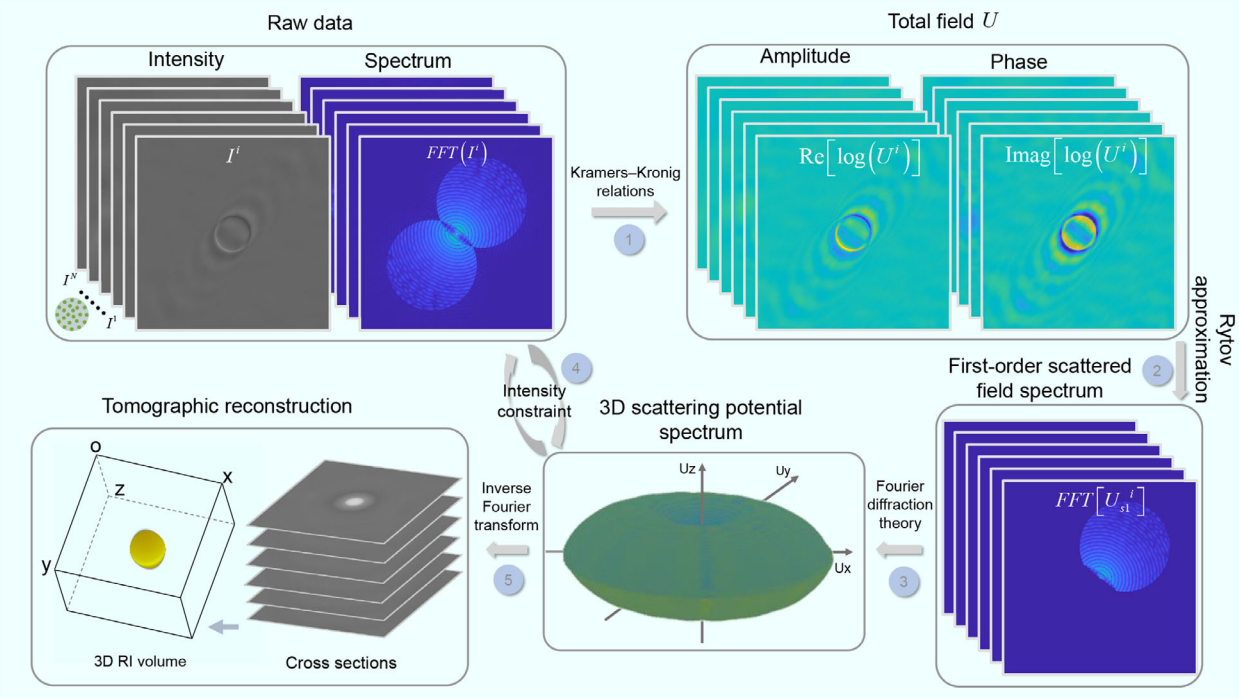

Figure 2. Workflow of KK-FPDT (summarized in Supporting Video S1). Multiple images captured under varied LED illumination. Complex field reconstruction by KK relations. The complex field at each angle is mapped into 3D Fourier space to generate an initial scattering potential spectrum distribution. An iterative intensity constraint algorithm is implemented on the estimated scattering potential spectrum. Deconvolution was implemented on the 3D scattering potential spectrum to obtain the 3D RI distribution of the samples.

lar spheres and compared it with the conventional KK-ODT and FPDT, as described in Supporting Information S4.

To ensure the validity of our method under the first-order Rytov approximation, we have prudently designed the parameters of the simulated samples. Given that typical biological cells have a thickness of approximately 10 μm and a RI difference of about 0.02 to 0.04 relative to the surrounding medium, which approximately satisfies the conditions for applying the Rytov approximation in weakly scattering regimes.[21,40] Therefore, we designed the simulated phase microspheres to have a diameter of 12 μm and a RI of 1.60 ($\lambda = 0.507$ μm) in a medium with a RI of 1.58. In the simulation, KK-FPDT and KK-ODT illuminated microspheres using 128 and 45 incident waves, respectively. These waves were arranged in a regular concentric circular pattern within k-space and had a maximum NA_{ill} of 0.75.

Figure 3a shows the 45 intensity images of microsphere captured under matched illumination. It also presents the amplitude and phase distributions of the total field reconstructed using KK relations under matched illumination, as well as the reconstructed RI and scattering potential spectrum distributions of the microspheres with KK-ODT. Since the finite illumination angle, the KK-ODT only accesses a small amount of the scattering potential spectrum of the microspheres leading to an underestimation of the reconstructed RI. Furthermore, the background of the reconstructed x-z and y-z slices suffers from more unwanted contrast. Figure 3b shows the 128 intensity images of microspheres captured under full-angle illumination, and it also presents the amplitude and phase distributions of the total field reconstructed using KK relations under non-matched illumination. Moreover, the reconstructed RI and scattering potential spectrum distributions of the microspheres obtained with KK-FPDT are displayed in this figure. In contrast, KK-FPDT recovers RI with a more uniform background, which is similar to the ground truth. To quantitatively evaluate the reconstruction performance of the two methods, we plotted RI line profiles across different cross-sectional planes (Figure 3c). All metrics show that KK-FPDT exhibits superior reconstruction performance compared to KK-ODT reconstruction. However, both techniques suffer from missing-cone issues due to the limited illumination angle. To address this, a non-negative constrained iteration-based post-processing algorithm is applied. It fills the missing-cone areas in the 3D Fourier spectrum of KK-FPDT's simulation results, achieving a 3D RI reconstruction that aligns with the theoretical RI value of 1.6 (Figure 3d). Furthermore, we show the RI distributions of multicellular spheroids reconstructed with KK-ODT, FPDT and KK-FPDT, respectively, in Supporting Information S4. The results show that FPDT and KK-FPDT exhibited superior reconstruction performance compared to KK-ODT. Moreover, KK-FPDT shows superior reconstruction quality compared to FPDT for the same number of iterations because of the lack of initial estimation in FPDT, which highlights the advantage of fast and stable convergence of KK - FPDT.

3.2. Hardware Implementation for KK-FPDT

We experimentally verified our technique using an Olympus IX83 inverted microscope outfitted with a ring LED array, as

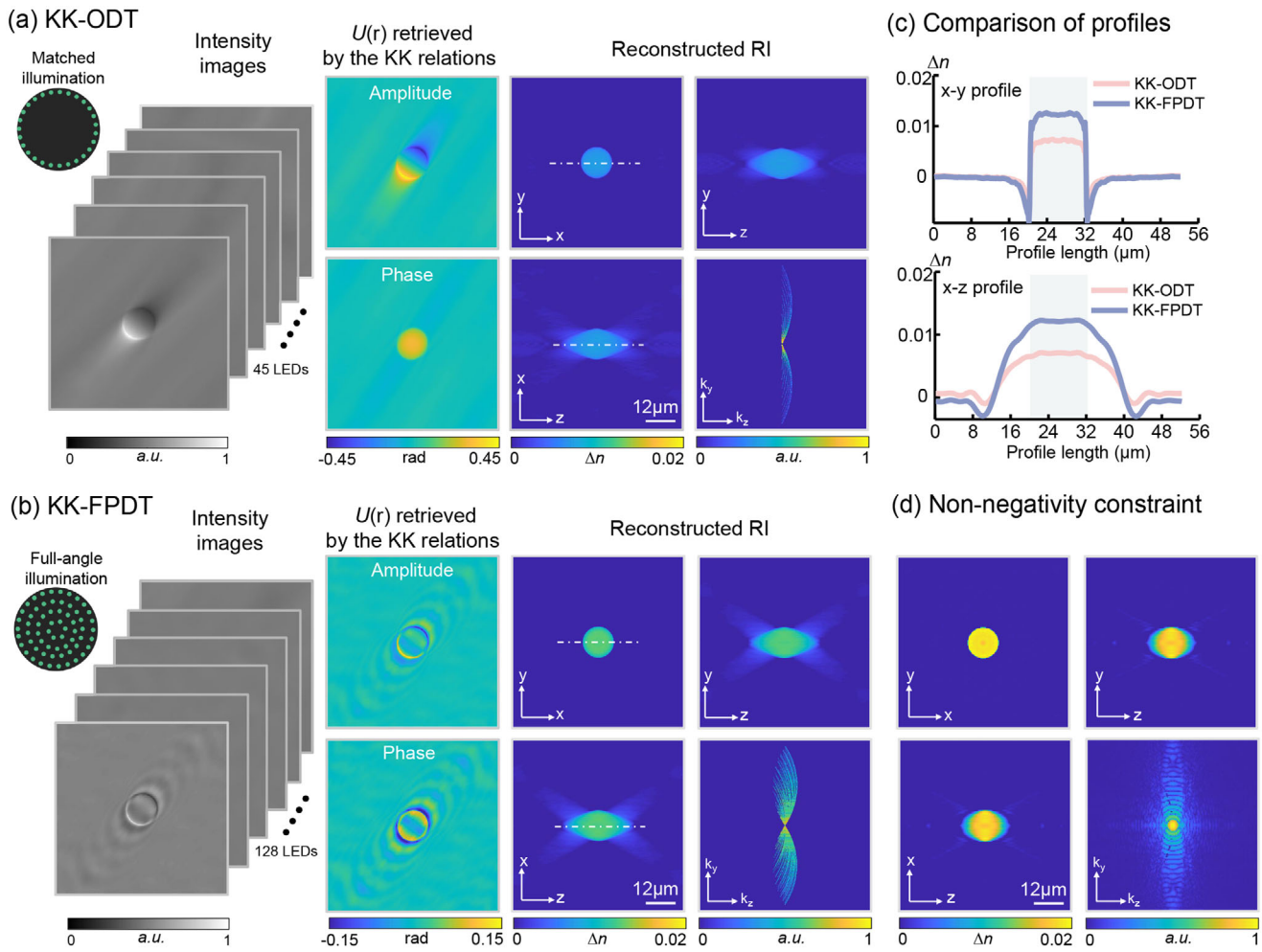

Figure 3. Simulations comparing the 3D RI reconstructions using the KK-ODT and KK-FPDT. a) Optical tomographic reconstruction of a simulated microsphere employing the KK-ODT. Intensity images of microsphere measured under 45 matched illuminations. Wavefront reconstruction of complex field via KK relations under matched illumination. Orthogonal RI slices and the scattering potential spectrum of microsphere reconstructed by KK-ODT. b) Optical tomographic reconstruction of a simulated microsphere employing the KK-FPDT. Intensity images of microsphere measured under 128 matched and non-matched illuminations. Wavefront reconstruction of complex field via KK relations under non-matched illumination. Orthogonal RI slices and the scattering potential spectrum of microsphere reconstructed by KK-FPDT. c) The profile of the microsphere along the white dashed lines are plotted in the x-y and x-z planes. d) Orthogonal RI slices and scattering potential spectrum of simulated microsphere reconstructed with non-negativity iterative constraints based on KK-FPDT results.

shown in **Figure** 4a. The microscope uses an infinity corrected objective lens (40×/0.75 UPlanSApo, Olympus) and a CMOS camera containing 6.5 μm pixels (Hamamatsu ORCA-Flash 4.0 C13440, 2048 × 2048 pixel count). The LED array, consisting of six integrated LED rings of different diameters, is aligned with the microscope's optical axis and positioned 60 mm from the sample to achieve a maximum NA_{ill} of 0.75. Each LED unit is sequentially activated by the ARM board controller, generating spatially coherent quasi-monochromatic illumination centered at 507 nm. Employing the parameters of $NA_{ill} = 0.75$ and $NA_{obj} = 0.75$ as well as the theoretical full-width lateral and axial resolution definition formulas

$$\Delta x, y = \frac{\lambda}{\mathrm{NA}_{ill} + \mathrm{NA}_{obj}}, \ \Delta z = \frac{\lambda}{1 - \sqrt{1 - \mathrm{NA}_{ill}{}^2}} \tag{6}$$

it can be calculated that the lateral resolution is 0.338 μm and axial resolution is 1.49 μm. For the KK-FPDT and FPDT reconstructions, we capture and processes 132 intensity images under full-angle illumination. For the KK-ODT reconstruction, we capture 40 intensity images under matched illumination. All the experimental data are processed based on MATLAB software (MATLAB R2023b) with a computer workstation (Intel Core i7-10870H, 2.20GHz central processing unit, 64 GB random-access memory).

3.3. Validation of KK-FPDT on Experiments

To experimentally demonstrate the performance of KK-FPDT for quantitative 3D RI reconstruction, we performed diffraction tomography on a 10 μm polystyrene bead. The bead has an ideal

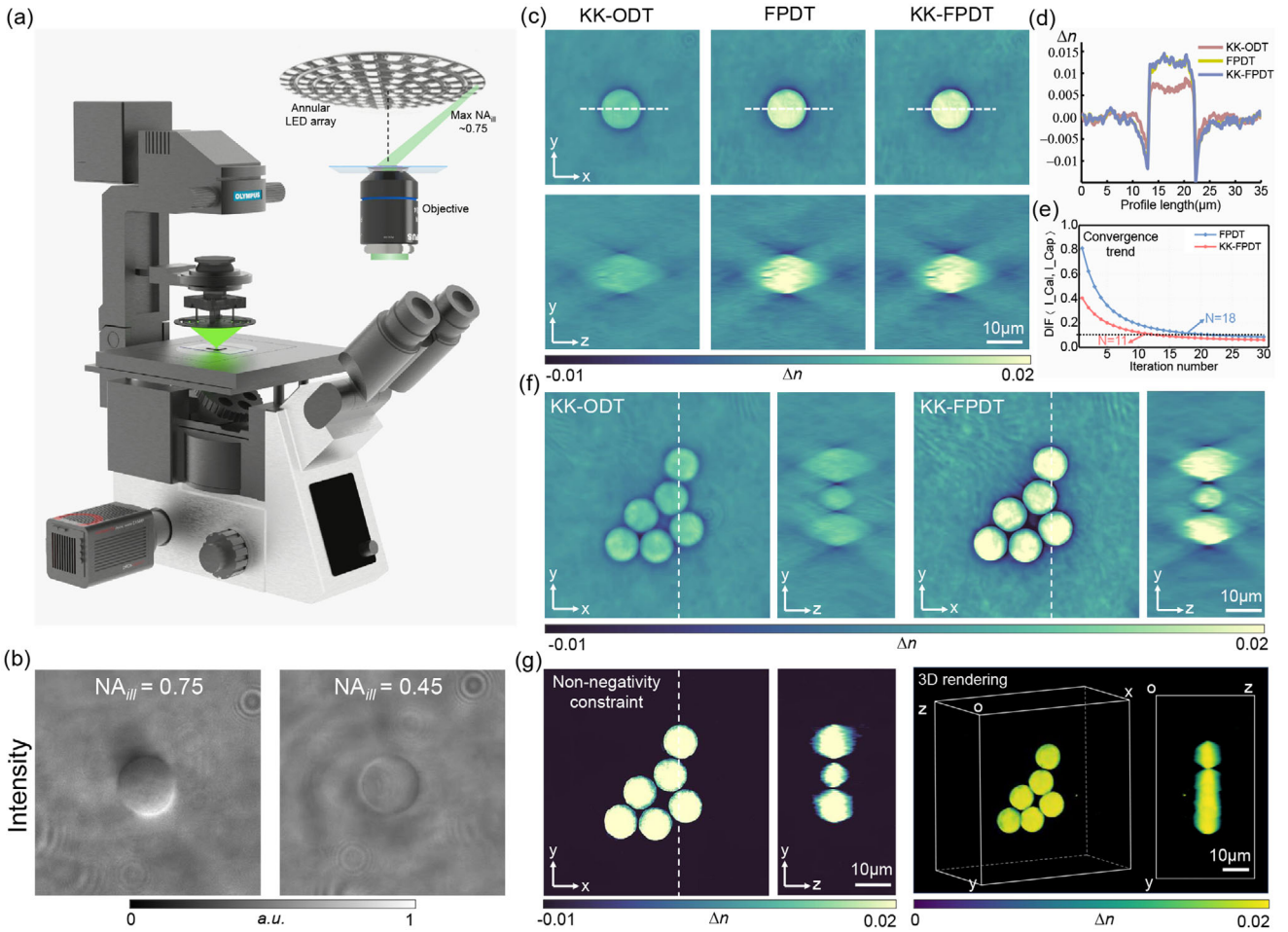

Figure 4. Optical setup of KK-FPDT platform and quantitative tomographic experimental results for polystyrene bead. a) Schematic diagram of the illumination and imaging system of the KK-FPDT platform. The light source of an off-the-shelf inverted microscope (IX83, Olympus, Japan) is replaced by an LED array. b) Distribution of measured intensity of polystyrene bead with 10 μm diameter under two different illumination angles. c) Orthogonal slices of 3D RI reconstructions of single polystyrene bead from KK-FPDT and other 3D imaging methods (KK-ODT and FPDT). d) The profile of polystyrene bead along the white dashed lines are plotted in the x-y plane. e) Difference between the calculated and measured intensities for the KK-FPDT and FPDT during the iteration process. f) Orthogonal slices of 3D RI reconstructions of polystyrene bead cluster from KK-FPDT and KK-ODT. g) Orthogonal RI slices of reconstructed polystyrene bead cluster with nonnegativity iterative constraint based on the result of KK-FPDT in the experiment. 3D rendering of the reconstructed polystyrene bead are plotted on the right side.

RI of 1.6 and was immersed in a matching medium ($n_m = 1.58$). In the experiment, 132 incident angles were used with the maximum NA_{ill} matching the NA_{obj}. Additionally, we employed KK-ODT and FPDT for comparative reconstructions. Figure 4b illustrates the intensity distribution of beads under two different illumination angles. Under matched illumination, strong phase contrast is evident in the intensity image. The degradation of low-frequency phase information under non-matched illumination is consistent with the POTF theory. The RI reconstructions in x-y and x-z planes using the three techniques are displayed in Figure 4c. Due to the use of only 40 intensity images with matched illumination in KK-ODT, the resulting RI is significantly underestimated and exhibits low contrast, consistent with our simulations. In contrast, beads reconstructed using FPDT and KK-FPDT display higher RI values and contrast. The beads are elongated in the z-direction in all three techniques because of the missing-cone of scattering potential, as illustrated in the x-z plane diagram. Figure 4d presents the lateral profile curves of RI for a quantitative assessment of the reconstruction performance across the three techniques. FPDT and KK-FPDT demonstrate similar reconstruction performance due to their use of an equivalent number of intensity images, outperforming KK-ODT in terms of reconstruction quality. The convergence performance of FPDT and KK-FPDT is evaluated using the discrepancy between computed and measured intensities, as depicted in Figure 4e. As observed from Figure 4e, the convergence times of KK-FPDT and FPDT were approximately 11 and 18 iterations, respectively. Furthermore, the time required for single-iteration reconstruction was calculated to be 1.25 s for KK-FPDT and 1.27 s for FPDT. In conventional FPDT, the iterative process often shows slow convergence due to the substantial difference between the initial zero value and the true RI to be determined. Conversely, KK-FPDT displays a faster convergence trend, attributed to the initial RI estimation via the KK relations. Overall, the total reconstruction

times were approximately 15.07 s for KK-FPDT (including 1.32 s for initialization and 13.75 s for iteration) and 22.90 s for FPDT. In conventional FPDT, the iterative process often shows slow convergence and stagnation due to the substantial difference between the initial zero value and the true RI to be determined. Conversely, KK-FPDT displays a faster and more stable convergence trend, attributed to the initial RI estimation via the KK relations. Figure 4f further highlights KK-FPDT's superior 3D RI reconstruction capability by comparing its tomographic results of polystyrene bead clusters with those from KK-ODT. Finally, a post-processing algorithm based on non-negative constrained iterations is applied to the results of the polystyrene bead clusters reconstructed using KK-FPDT to reduce axial elongation, as illustrated in Figure 4g. The rendered 3D volumetric RI distribution of the bead cluster was presented on the right side of Figure 4g and animated in Supporting Video S2.

The superior reconstruction performance of KK-FPDT is realized through the integration of initial RI estimation with the FPDT iterative framework. In Supporting Information S5, we imaged a USAF target to characterize the imaging resolution of KK-FPDT. Figure S3a shows the lateral and axial RI slices of the USAF target reconstructed using KK-FPDT. The theoretical lateral resolution of the KK-FPDT system is approximately 338 nm, surpassing the minimum element of the USAF target (minimum 10-6, full cycle width 548 nm). Line profile analysis of the reconstructed minimum element of the USAF target indicates a lateral resolution of 560 nm, close to the theoretical full cycle width of 548 nm. For axial resolution, the maximum theoretical value for KK-FPDT is 1.49 μm. The line profile of the axial slice of the USAF target in Figure S3b shows a maximum full width of 1.80 μm, which deviates slightly from the theoretical prediction. This discrepancy is mainly attributed to the missing-cone problem in the direction near the low zero frequency area.

In Supporting Information S6, we used the USAF target to clearly illustrate the distinct roles of the initial RI estimate and the FPDT iterative framework within KK-FPDT. The results show that initial estimation using the KK relations mitigates RI underestimation to some extent, but may compromise the quality of low-frequency information. By subsequently applying the FPDT iterative framework, the RI distribution can be accurately reconstructed through multiple iterations. Figure S5 also compares the impact of KK-ODT and KK-FPDT on 3D RI reconstruction under the same number of illuminations (see Supporting Information S7). The results indicate that KK-FPDT achieves high-frequency reconstruction quality comparable to KK-ODT, while also exhibiting superior low-frequency reconstruction performance. Taken together, these results demonstrate that KK-FPDT possesses superior 3D RI restoration capabilities, overcoming the limitations of conventional KK-ODT in reconstructing RI under non-matched illumination conditions.

Subsequently, we performed a comprehensive validation of KK-FPDT's high-resolution tomographic imaging capability using diverse unlabeled transparent biological samples. It should be clarified that all biological samples used in this study were prepared entirely within our laboratory and did not involve any external sources or procurement. All experimental procedures were approved by the Institutional Biosafety Committee at Nanjing University of Science and Technology, and in tight accordance with relevant guidelines and regulations. As shown in **Figure 5**, we compared the KK-ODT with KK-FPDT for RI reconstruction (1350 × 1350 × 50 voxels) of weakly scattering fibroblast (3T3) cells. Fibroblasts are typically multinodular, spindle- or star-shaped flat cells characterized by regular ovoid nuclei and large conspicuous nucleoli. Although intracellular lipids and nucleoli can be resolved in KK-ODT, their contrasts vary weakly. However, the case of KK-FPDT showed a strong contrast in optically dense structures to clearly resolve intracellular structures such as lipids and nucleosomes (Figure 5a). Additionally, multinodular fusiform cells were observed in several regions of interest (ROIs), exhibiting long filamentous extensions. Figure 5b displays three lateral slices of ROI 1 at depths of z = −0.98 μm, 0 μm, and 0.98 μm, along with one axial slice at y = 0 μm. The filopodia were clearly visible in both KK-ODT and KK-FPDT at z = 0 μm. KK-ODT was almost impossible to distinguish filamentary detailed structures from the background of z = −0.98 μm, 0.98 μm slices, whereas KK-FPDT significantly improved the visibility of filamentary structures and achieved a higher resolution than KK-ODT. Figure 5c presents a comparison of the profiles of filamentous structures at various depths for both methods. The lateral full width at half maximum of the filamentary structure was measured at 0.48 μm, demonstrating KK-FPDT's high-resolution imaging capability. Figure 5d shows maximum intensity projection (MIP) of ROI 1, clearly capturing the morphological distribution of filamentous structures. ROIs 2 and 3 are further enlarged in Figure 5e to better demonstrate cell morphology details across various axial planes (see Supporting Video S3 for 3D ROIs RI stack of 3T3 cell). The line contours spanning the submicron-scale organelles exhibit a lateral resolution close to the diffraction limit of 340 nm, as shown in Figure 5f. Figure 5g shows the MIP of ROI3, clearly capturing the long filopodial extensions of 3T3 cells. Additional RI tomograms of a variety of different cells types reveals strikingly different morphologies (A549 cells, H9C2 cardiomyocytes, see Supporting Information S8).

To demonstrate the tomographic performance of KK-FPDT for thick samples, we imaged two *Pandorina morum* algae (*P. morum*) located at various depths. *P. morum* are multicellular clusters, which can be viewed as a weakly scattering sample due to their non-dense structure. **Figure 6**a presents the raw intensity measurements of *P. morum* under three different illumination angles. It can be clearly observed from Figure 6a that the multicellular structure of *P. morum* leads to significant intensity contrast even when illuminated at small angles. Figure 6b presents lateral slices at different depths from the 3D RI reconstructions of *P. morum*. These slice diagrams allow us to discern the structural components of *P. morum*. Each *P. morum* consists of multiple cellular units that coalesce to form a spherical colony. High-RI particle-like structures are unevenly distributed around these cellular units. Moreover, each *P. morum*'s middle RI slice exhibits a complete edge contour. As imaging depth increased, the contours became blurred or vanished altogether. Notably, while internal cellular units are discernible at imaging depths of –9.75 μm and 8.13 μm, reconstructing high-frequency details like particle-like structures becomes impractical. Although *P. morum* is a weak scattering sample, multiple scattering effects still intensify with imaging depth. Since KK-FPDT only accounts for single scattering, the intensity variations from multiple scattering introduce noise and artifacts into the reconstruction. Consequently,

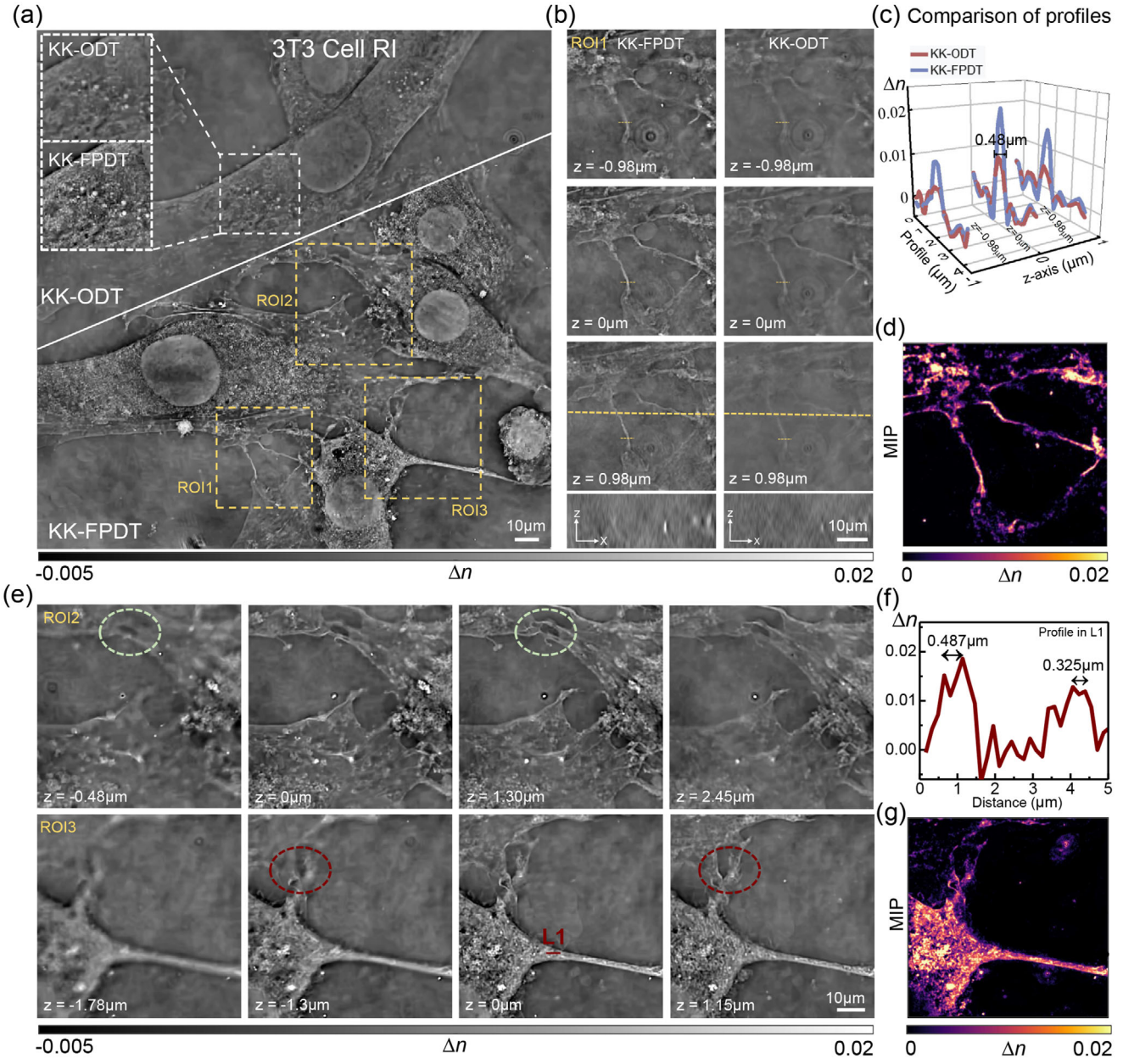

Figure 5. 3D RI reconstruction of 3T3 cells using KK-FPDT and KK-ODT. a) Comparison among the results of tomography of 3T3 cell utilizing KK-ODT (upper) and KK-FPDT (lower). b) Comparison of the reconstruction results of T3T cells by two techniques at three different depths. c) RI line profiles at three depths compare the reconstruction performance of the two techniques. d) MIP of reconstructed RI map in ROI1. e) x-y cross-sectional views of two different tomogram ROIs at different axial planes. f) Line profiles across subcellular structures to quantify the reconstructed resolution. g) MIP of reconstructed RI map in ROI3.

stronger multiple scattering leads to more severe RI underestimation and lower imaging resolution. Figure 6c shows the 3D rendering of *P. morum*. The recovered through-slice RI stacks of P. morum and their corresponding 3D rendered images are animated in Supporting Video S6.

4. Conclusion

In summary, we have introduced KK-FPDT, a high-efficiency tomography method for reconstructing the 3D RI distribution of unstained specimens. It employs 2D spatial-domain KK relations to reconstruct 3D RI distributions from intensity images captured under various illumination angles, including both matched and non-matched illuminations. KK-FPDT eliminates the need for matched illumination, allowing the use of scattered field information from any illumination angle to fill the 3D scattering potential spectrum. This improvement enhances the quality of RI reconstruction, making KK-FPDT more versatile than KK-ODT. Furthermore, KK-FPDT converges faster than FPDT, thanks to its initial estimation of the 3D RI distribution. Experimental re-

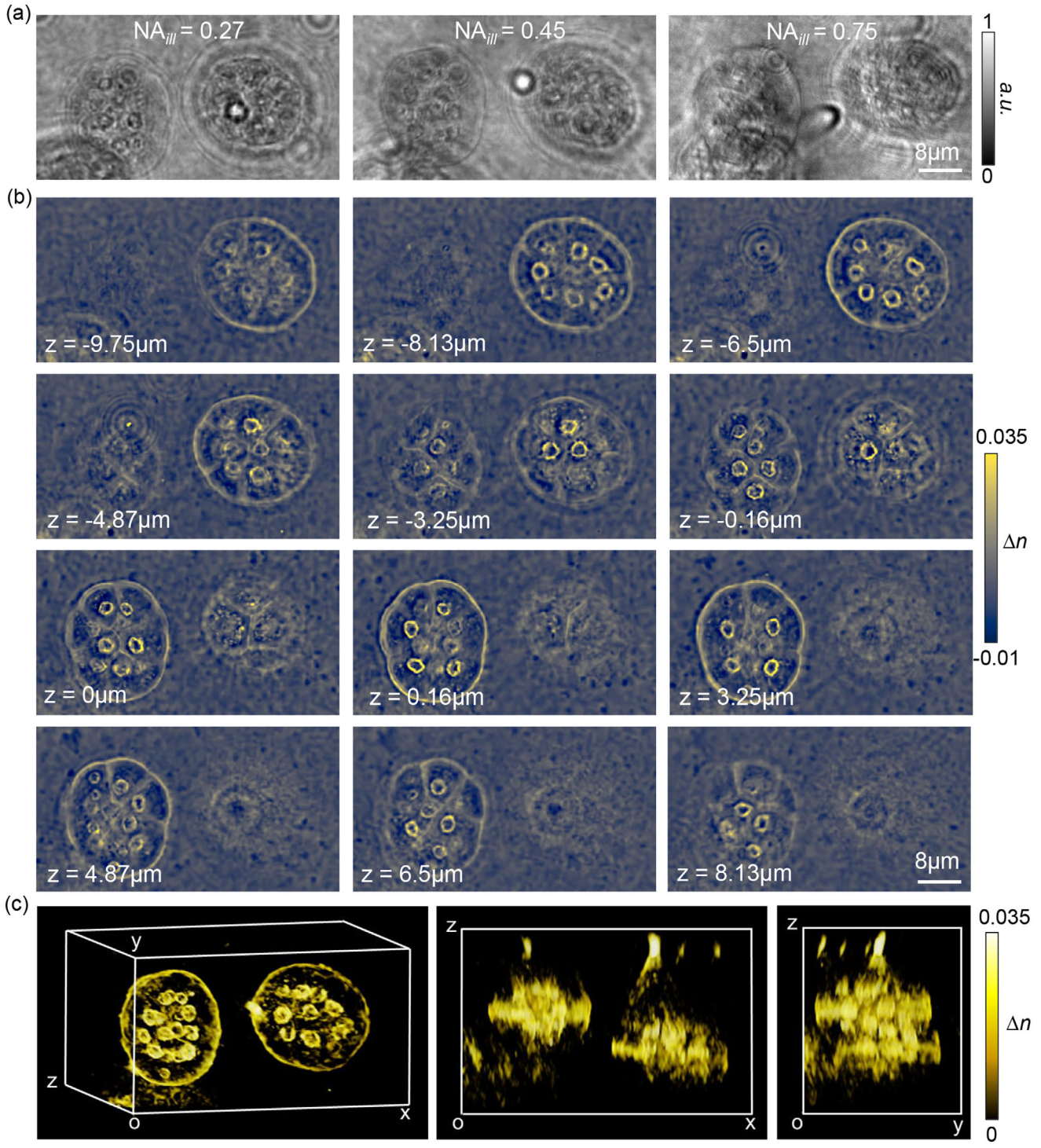

Figure 6. 3D quantitative RI reconstruction of P. morum using KK-FPDT. a) Raw intensity acquisitions at varying illumination angles. b) Lateral slices through the 3D RI reconstruction volume at different axial positions. c) 3D RI rendering of the P. morum.

sults with various samples, including polystyrene beads, USAF targets, and fixed cells, confirmed the high-resolution 3D imaging capabilities of KK-FPDT. We anticipate that this method will serve as a powerful tool for quantitatively analyzing cellular and tissue morphological changes.

Despite its effectiveness, KK-FPDT faces several inherent limitations. First, it is fundamentally based on the Rytov approximation, which assumes weak scattering of samples. This assumption may not hold for samples exhibiting strong scattering or large RI contrasts, potentially leading to inaccuracies in modeling

the scattered field. To address this, future work should explore more sophisticated forward models that incorporate multiple scattering effects which would enhance the accuracy and imaging depth of KK-FPDT.[42–45] Second, imaging performance is restricted by the finite NA of the objective lens and limited illumination angles. These constraints result in the missing-cone problem, which leads to anisotropic resolution and incomplete reconstruction of high spatial frequencies.[46,47] Although we have applied a non-negative iterative constraint algorithm to partially compensate for this deficiency, additional algorithmic and optical improvements are still needed.[6,48–51] Furthermore, integrating dark-field illumination into the KK-FPDT framework can provide complementary high-angle scattering information,[31,52] offering the potential to further enhance the resolution and contrast of the reconstructed RI distributions.

Supporting Information

Supporting Information is available from the Wiley Online Library or from the author.

Acknowledgements

This work was supported by the National Natural Science Foundation of China (62227818, 62361136588, 62305162, U21B2033), National Key Research and Development Program of China (2022YFA1205002, 2024YFE0101300, 2024YFF0505603, 2024YFF0505600), Biomedical Competition Foundation of Jiangsu Province (BE2022847), Key National Industrial Technology Cooperation Foundation of Jiangsu Province (BZ2022039), Fundamental Research Funds for the Central Universities (30923010206), Fundamental Research Funds for the Central Universities (2023102001, 2024202002), National Key Laboratory of Plasma Physics (JCKYS2024212804), and Open Research Fund of Jiangsu Key Laboratory of Spectral Imaging & Intelligent Sense (JSGP202105, JSGP202201, JSGPCXZNGZ202401).

Conflict of Interest

The authors declare no conflict of interest.

Author Contributions

First and second author, Z.B. and S.Z., are co-first authors. Z.B. and S.Z. contributed equally to this work. Z.B. and S.Z. developed the theoretical description of the method; Z.B. and H.U. performed experiments; Z.B. analyzed the data. Z.B., S.Z., L.L., H.U. and R.Y. participated in discussions during the development of the paper; Q.C. and C.Z. conceived and supervised the research; All authors contributed to writing and correcting the manuscript.

Data Availability Statement

The data that support the findings of this study are available from the corresponding author upon reasonable request.

Keywords

Fourier ptychographic diffraction tomography, Kramers–Kronig relations, optical diffraction tomography

Received: March 28, 2025
Revised: June 17, 2025
Published online:

[1] Y. Park, C. Depeursinge, G. Popescu, *Nat. Photonics* **2018**, *12*, 578.
[2] Y. Cotte, F. Toy, P. Jourdain, N. Pavillon, D. Boss, P. Magistretti, P. Marquet, C. Depeursinge, *Nat. Photonics* **2013**, *7*, 113.
[3] W. Choi, C. Fang-Yen, K. Badizadegan, S. Oh, N. Lue, R. R. Dasari, M. S. Feld, *Nat. Methods* **2007**, *4*, 717.
[4] J. Yoon, Y. Jo, M.-h. Kim, K. Kim, S. Lee, S.-J. Kang, Y. Park, *Sci. Rep.* **2017**, *7*, 6654.
[5] K. Kim, J. Yoon, S. Shin, S. Lee, S.-A. Yang, Y. Park, *J. Biomedical Photon. Engineering* **2016**, *2*, 2.
[6] F. Merola, P. Memmolo, L. Miccio, R. Savoia, M. Mugnano, A. Fontana, G. D'ippolito, A. Sardo, A. Iolascon, A. Gambale, P. Ferraro, *Light: Sci. Appl.* **2017**, *6*, e16241.
[7] T. L. Nguyen, S. Pradeep, R. L. Judson-Torres, J. Reed, M. A. Teitell, T. A. Zangle, *ACS Nano* **2022**, *16*, 11516.
[8] J. Rosen, S. Alford, B. Allan, V. Anand, S. Arnon, F. G. Arockiaraj, J. Art, B. Bai, G. M. Balasubramaniam, T. Birnbaum, N. S. Bisht, D. Blinder, L. Cao, Q. Chen, Z. Chen, V. Dubey, K. Egiazarian, M. Ercan, A. Forbes, G. Gopakumar, Y. Gao, S. Gigan, P. Goclowski, S. Gopinath, A. Greenbaum, R. Horisaki, D. Ierodiaconou, S. Juodkazis, T. Karmakar, V. Katkovnik, *Appl. Phys. B* **2024**, *130*, 166.
[9] L. Tian, L. Waller, *Optica* **2015**, *2*, 104.
[10] R. Horstmeyer, J. Chung, X. Ou, G. Zheng, C. Yang, *Optica* **2016**, *3*, 827.
[11] R. Ling, W. Tahir, H.-Y. Lin, H. Lee, L. Tian, *Biomed. Opt. Express* **2018**, *9*, 2130.
[12] J. Li, A. Matlock, Y. Li, Q. Chen, C. Zuo, L. Tian, *Adv. Photonics* **2019**, *1*, 066004.
[13] C. Zuo, J. Sun, J. Li, A. Asundi, Q. Chen, *Optics Lasers Engineering* **2020**, *128*, 106003.
[14] A. Pan, C. Zuo, B. Yao, *Rep. Prog. Phys.* **2020**, *83*, 096101.
[15] N. Streibl, *J. Opt. Soc. Am. A* **1985**, *2*, 121.
[16] M. Chen, L. Tian, L. Waller, *Biomed. Opt. Express* **2016**, *7*, 3940.
[17] J. M. Soto, J. A. Rodrigo, T. Alieva, *Opt. Express* **2017**, *25*, 15699.
[18] J. Li, Q. Chen, J. Sun, J. Zhang, J. Ding, C. Zuo, *Biomed. Opt. Express* **2018**, *9*, 2526.
[19] C. Zuo, J. Li, J. Sun, Y. Fan, J. Zhang, L. Lu, R. Zhang, B. Wang, L. Huang, Q. Chen, *Optics and Lasers in Engineering* **2020**, *135*, 106187.
[20] Y. Chung, H. Hugonnet, S.-M. Hong, Y. Park, *Opt. Express* **2024**, *32*, 18790.
[21] Y. Sung, W. Choi, C. Fang-Yen, K. Badizadegan, R. R. Dasari, M. S. Feld, *Opt. Express* **2009**, *17*, 266.
[22] J. M. Soto, J. A. Rodrigo, T. Alieva, *Appl. Opt.* **2018**, *57*, A205.
[23] U. S. Kamilov, I. N. Papadopoulos, M. H. Shoreh, A. Goy, C. Vonesch, M. Unser, D. Psaltis, *IEEE Transactions on Computational Imaging* **2016**, *2*, 59.
[24] J. Lim, A. B. Ayoub, E. E. Antoine, D. Psaltis, *Light: Sci. Appl.* **2019**, *8*, 82.
[25] S. Chowdhury, M. Chen, R. Eckert, D. Ren, F. Wu, N. Repina, L. Waller, *Optica* **2019**, *6*, 1211.
[26] W. Pierré, L. Hervé, C. Paviolo, O. Mandula, V. Remondiere, S. Morales, S. Grudinin, P. F. Ray, M. Dhellemmes, C. Arnoult, C. Allier, *Appl. Opt.* **2022**, *61*, 3337.
[27] U. S. Kamilov, I. N. Papadopoulos, M. H. Shoreh, A. Goy, C. Vonesch, M. Unser, D. Psaltis, *Optica* **2015**, *2*, 517.
[28] M. Chen, D. Ren, H.-Y. Liu, S. Chowdhury, L. Waller, *Optica* **2020**, *7*, 394.
[29] A. Saba, C. Gigli, A. B. Ayoub, D. Psaltis, *Adv. Photonics* **2022**, *4*, 066001.
[30] S. Zhou, J. Li, J. Sun, N. Zhou, H. Ullah, Z. Bai, Q. Chen, C. Zuo, *Optica* **2022**, *9*, 1362.
[31] S. Zhou, J. Li, J. Sun, N. Zhou, Q. Chen, C. Zuo, *Journal of Biophotonics* **2022**, *15*, e202100272.

[32] Y. Baek, Y. Park, *Nat. Photonics* **2021**, *15*, 354.
[33] R. De L. Kronig, *J. Opt. Soc. Am.* **1926**, *12*, 547.
[34] C. Lee, Y. Baek, H. Hugonnet, Y. Park, *Opt. Lett.* **2022**, *47*, 1025.
[35] J. Sun, C. Zuo, J. Zhang, Y. Fan, Q. Chen, *Sci. Rep.* **2018**, *8*, 7669.
[36] J. Li, N. Zhou, J. Sun, S. Zhou, Z. Bai, L. Lu, Q. Chen, C. Zuo, *Light: Sci. Appl.* **2022**, *11*, 154.
[37] J. Wang, X. Zhao, Y. Wang, D. Li, *Photonics Res.* **2024**, *12*, 2712.
[38] E. Wolf, *Opt. Commun.* **1969**, *1*, 153.
[39] V. Lauer, *J. Microsc.* **2002**, *205*, 165.
[40] A. Devaney, *Opt. Lett.* **1981**, *6*, 374.
[41] V. Mico, Z. Zalevsky, P. García-Martínez, J. García, *J. Opt. Soc. Am. A* **2006**, *23*, 3162.
[42] U. S. Kamilov, D. Liu, H. Mansour, P. T. Boufounos, *IEEE Signal Processing Letters* **2016**, *23*, 1052.
[43] H.-Y. Liu, D. Liu, H. Mansour, P. T. Boufounos, L. Waller, U. S. Kamilov, *IEEE Transactions on Computational Imaging* **2017**, *4*, 73.
[44] J. Lim, A. Goy, M. H. Shoreh, M. Unser, D. Psaltis, *Phys. Rev. Appl.* **2018**, *9*, 034027.
[45] M. Lee, H. Hugonnet, Y. Park, *Optica* **2022**, *9*, 177.
[46] F. Macias-Garza, K. R. Diller, A. C. Bovik, *Optical Engineering* **1988**, *27*, 461.
[47] B. Simon, M. Debailleul, M. Houkal, C. Ecoffet, J. Bailleul, J. Lambert, A. Spangenberg, H. Liu, O. Soppera, O. Haeberlé, *Optica* **2017**, *4*, 460.
[48] J. Lim, K. Lee, K. H. Jin, S. Shin, S. Lee, Y. Park, J. C. Ye, *Opt. Express* **2015**, *23*, 16933.
[49] K. C. Zhou, R. Horstmeyer, *Opt. Express* **2020**, *28*, 12872.
[50] M. Lee, K. Kim, J. Oh, Y. Park, *Light: Sci. Appl.* **2021**, *10*, 102.
[51] J. Wang, E. S. Allgeyer, G. Sirinakis, Y. Zhang, K. Hu, M. D. Lessard, Y. Li, R. Diekmann, M. A. Phillips, I. M. Dobbie, J. Ries, M. J. Booth, J. Bewersdorf, *Nat. Protoc.* **2021**, *16*, 677.
[52] G. Zheng, C. Kolner, C. Yang, *Opt. Lett.* **2011**, *36*, 3987.